Characterizing the performance of a POPS miniaturized optical particle counter when operated on a quadcopter drone

Zixia Liu[1], Martin Osborne[1,2], Jim Haywood[1,2], Karen Anderson[3], Jamie D. Shutler[3], Andy Wilson[2], Justin Langridge[2], Steve H.L. Yim[4,5,6,7], Hugh Coe[8], Suresh Babu[9], Sreedharan K. Satheesh[10], Paquita Zuidema[11], Tao Huang[4], Jack C.H. Cheng[4].

Affiliations:

[1]College of Engineering Mathematics, and Physical Sciences, University of Exeter, Exeter, Devon, UK

[2]Met Office, Fitzroy Road, Exeter, Devon, UK

[3]College of Life and Environmental Sciences, University of Exeter, Penryn, Cornwall, UK

[4]Department of Geography and Resource Management, The Chinese University of Hong Kong, Hong Kong, China

[5]Stanley Ho Big Data Decision Analytics Research Centre, The Chinese University of Hong Kong, Hong Kong, China

[6]Institute of Environment, Energy and Sustainability, The Chinese University of Hong Kong, Hong Kong, China

21   [7]Asian School of the Environment, Nanyang Technological University,

22   Singapore

23   [8]Department of Earth and Environmental Sciences, University of

24   Manchester, Manchester, UK

25   [9]Space Physics Laboratory, Vikram Sarabhai Space Centre, Trivandrum,

26   695 022, India

27   [10]Centre for Atmospheric and Oceanic Sciences, Indian Institute of Science,

28   Bangalore 560 012, India

29   [11]Rosenstiel School of Marine and Atmospheric Science, University of

30   Miami, Miami, FL, USA

31   *Correspondence to:* J. Haywood (J.M.Haywood@exeter.ac.uk)

32   **Abstract:**

33   We first validate the performance of the Portable Optical Particle Spectrometer (POPS),

34   a small light-weight and high sensitivity optical particle counter, against a reference

35   scanning mobility particle sizer (SMPS) for a month-long deployment in an

36   environment dominated by biomass burning aerosols. Subsequently, we examine any

37   biases introduced by operating the POPS on a quadcopter drone, a DJI Matrice 200 V2.

38   We report the root mean square difference (RMSD) and mean absolute difference

39   (MAD) in particle number concentrations (PNCs) when operating on the ground and

40   on the drone. When windspeeds are low (less than 2.6 m/s), we find only modest

41   differences in the RMSDs and MADs of 5% and 3% when operating at 10m altitude.

42   When windspeeds are between 2.6 - 7.7m/s the RMSDs and MADs increase to 26.2%

43   and 19.1%, respectively when operating at 10m altitude. No statistical difference in

44   PNCs was detected when operating on the UAV in either ascent or descent. We also

find size distributions of aerosols in the accumulation mode (defined by diameter, d, where $0.1 \leq d \leq 1\mu m$) are relatively consistent between measurements at the surface and measurements at 10m altitude while differences in the coarse mode (here defined by $d > 1\mu m$) are universally larger. Our results suggest that the impact of the UAV rotors on the POPS PNCs are small at low windspeeds, but when operating under higher wind speed of up to 7.6m/s, larger discrepancies occur. In addition, it appears that the POPS measures sub-micron aerosol particles more accurately than super-micron aerosol particles when airborne on the UAV. These measurements lay the foundations for determining the magnitude of potential errors that might be introduced into measured aerosol particle size distributions and concentrations owing to the turbulence created by the rotors on the UAV.

1 Introduction

Atmospheric aerosols have a significant impact on Earth's climate as they affect the radiative balance of the Earth-Atmosphere system through the direct effect which refers to absorption and scattering of solar and terrestrial radiation, and the indirect effect which refers to the ability of aerosols acting as condensation nuclei (CCN) (Haywood and Boucher, 2000; Boucher et al., 2013). Aerosol concentration and their intrinsic properties are spatially inhomogeneous owing to different emission sources, deposition processes, transports, and chemical reactions (e.g. Bellouin et al., 2005; Jiminez et al., 2009; Lack and Cappa, 2010; Atkinson et al., 2018; Yim et al., 2019; Yim et al., 2020).

Among these properties, particle size distributions (PSDs) and number concentrations (PNCs) are of fundamental importance in determining the impact of aerosols on the

68 atmospheric radiation budget via the aerosol direct and indirect effects. Based on

69 observations of the size distributions of aerosols and aerosol refractive index, aerosol

70 optical properties can be inferred (e.g. Atkinson et al., 2015). The size of aerosol

71 particles is also of primary importance in cloud formation and precipitation (Yin et al.,

72 2000; Liu et al., 2018; 2019a). As a result, in order to better understand the effect of

73 aerosols on climate change, it is important to obtain a comprehensive and accurate

74 characterization of the spatial distribution of aerosol concentration and properties.

75 Aerosols can also impact atmospheric visibility (e.g. Horvath, 1981), air quality, and

76 health (e.g. Li et al., 2003; Gu et al., 2016; 2018; 2020; Shi et al., 2019). In terms of

77 scales, satellite observations (e.g. Bellouin et al., 2005) are able to provide near global

78 coverage of aerosol optical depths, but are only able to provide bulk measurements of

79 properties of the aerosol size distribution (e.g. fine mode fraction) and aerosol optical

80 properties (e.g. aerosol absorption). Dedicated field sites (e.g. Zuidema et al., 2016,

81 2018) or dedicated sampling with aircraft instrumentation (e.g. Haywood et al., 2003a;

82 2020) are able to make much more detailed aerosol microphysical measurements, but

83 are costly and aircraft cannot sample aerosols at low altitude in built-up urban regions

84 owing to obvious safety concerns.

85

86 The atmospheric science community frequently utilizes optical particle counters (OPCs)

87 and Mie scattering theory for sizing individual aerosol particles (e.g. Burkhart et al.,

88 2010). Measurements of aerosols by small, unmanned aerial vehicles (UAVs) have

89 many advantages, such as low-cost, ease and cost of deployment, and ease of access to

90 inaccessible areas such as those close to urban conurbations. However, owing to

91 payload restrictions, UAVs require light-weight, minaturized OPCs. The Portable

92 Optical Particle Spectrometer (POPS) is an advanced and small low-cost, light-weight,

93 and high-sensitivity OPC, particularly designed for UAVs and balloon sondes (Gao et

94 al., 2013; 2016). In brief, the POPS samples particles by drawing air through an inlet

95 tube into an optical chamber, where it is illuminated by a 405nm laser. A sheath air

96 flow is used to focus the sample air into the centre of the laser beam, and the sample

97 flow is maintained at a near constant rate by an automatically regulated on-board pump.

98 Individual particle sizes are then inferred by comparing the recorded signal amplitudes

99 to scattering amplitudes calculated using Mie scattering theory.

100

101 The POPS has been carried by balloon sondes to study the vertical profile of the Asian

102 Tropopause Aerosol Layer (Yu et al., 2017), but quantitative data when deployed on a

103 quadcopter drone is very sparse. There have been some recent side-by-side tests of

104 miniaturized OPC instruments against more established instrumentation in controlled

105 environments. For example, Bezantakos et al. (2018) compared a newly developed

106 miniaturized OPC against a GRIMM OPC across a range of atmospheric conditions.

107 There have also been some very limited comparisons of miniaturized UAV-borne OPC

108 instrumentation against measurements on large atmospheric tower based

109 instrumentation (Ahn, 2019). Neither of these studies use the POPS OPC. Questions

110 about the impact of inlets, and aircraft boundary layer depths on aerosol measurements

have been the subject of research on aerosol for decades (Huebert et al., 1990; Sanchez-Marroquin, 2019). A similar significant question related to deploying the POPS instrument on a quadcopter drone is whether the turbulence generated by the multiple rotors and the attitude adjustment required to maintain positional stability impact the measurements of the aerosol concentrations and size distributions, and if so, to what extent. Here we provide the first comprehensive documentation of the performance of the POPS on a multi-rotor UAV. We first investigated the performance of the POPS instrument in a closely controlled environment on the ground in a three-week comparison of the POPS against reference instruments. The POPS was deployed at the Atmospheric Radiation Measurements (ARM) mobile facility on Ascension Island during colocation of the Layered Atlantic Smoke Interaction with Clouds (LASIC; Zuidema et al., 2016) and CLoud-Aerosol-Radiation Interaction and Forcing: Year-2017 (CLARIFY-2017; Haywood et al., 2020) measurement campaigns. Subsequently, when back in the UK, we examined the influence of the drone rotors and variability in the drone attitude on the measured aerosol number concentration and size distribution. Section 2 presents the methodology used in the ground-based comparison on Ascension Island. Section 2 also provides details of the methodology adopted for the UAV-mounted flights in UK. Section 3 presents the results before conclusions and future work is presented in section 4.

2 Methods

2.1 A 20-day comparison

As part of the CLARIFY-2017 and LASIC campaign, the POPS was deployed at the ARM mobile site on Ascension Island located in the mid-Atlantic (7.96° S, 14.37° W) alongside an ARM operated SMPS. The time period for sampling for both instruments analyzed here was from 20th August to 9th September 2017 (20 days) continuously, during which time biomass burning aerosol originating from the African continent was frequently present (Zuidema et al., 2018; Haywood, 2020). The SMPS and the POPS were connected to a common aerosol inlet, however, in the case of the SMPS, the sample air was dried before it entered the instrument.

In common with other OPCs, the POPS size distributions are influenced by the refractive index assumed in the Mie calculations. The manufacturer (Handix Scientific) provides a calibration for the POPS using well-sized latex spheres with a refractive index (RI) of 1.615+0.001i at 405 nm. Prior to deployment to Ascension Island, the manufacturer's calibration of the POPS was adjusted through independent lab-based measurements using latex spheres at the UK's Facility for Airborne Atmospheric Research (FAAM, https://www.faam.ac.uk/). Errors in the PSDs can be caused by sampling aerosols with a different refractive index to that of latex, particularly if they are significantly absorbing (e.g. Haywood et al., 2003). The independent lab-based calibration binning criteria were therefore adjusted assuming a RI of 1.54+0.027i at 405 nm, which is expected to be more representative of the biomass burning aerosol

152 particles sampled at the ARM site during the CLARIFY deployment (Peers et al., 2019).

153 In contrast to the optical sizing nature of the POPS, the SMPS that was operated by the

154 ARM mobile Facility uses particle mobility subsequent to application of an electrostatic

155 charge to size aerosol particles, a method which is independent of the refractive index

156 (Ruzer and Harley, 2012).

157

158 In addition to applying fundamentally different methods to measure the size of particles,

159 the POPS and SMPS cover different ranges of size distributions. The POPS measures

160 particles within the diameter range from around $0.12 - 4.44\mu m$ (for RI = 1.54+0.027i

161 at 405 nm), while the SMPS covers diameter ranging from around 0.01 to 1.00μm.

2.2 Drone-mounted POPS

163 The POPS required a carefully designed bespoke rig to fit it safely to a quadcopter

164 drone for deployment. A DJI Matrice 200 V2 was used because it had a sufficient power

165 and payload capacity to lift the POPS and even with the relatively high payload could

166 offer reasonable endurance. The maximum flight time of the Matrice is 24 minutes with

167 the maximum payload (1.45kg). University of Exeter and Met Office staff designed and

168 fitted the POPS to the Matrice airframe (Figure 1). The POPS was installed at the

169 bottom left of the fuselage and fixed on the customized 3-D printed landing gear. The

170 inlet tube of the POPS (red oval in Figure 1) reached 20cm above the rotors. The

171 diameter of the inlet tube is 1mm and the sample flow rate is 3 cm^3/s, yielding a flow

172 velocity of 3.8m/s. No attempt has been made to optimise this simple tube inlet for

173   drone applications. The data were collected during 14 test flights in total from 18th

174   December 2019 to 9th March 2020 to determine any impact of the rotors and attitude of

175   the UAV on the data from the POPS. Each test flight was planned to be separated into

176   three stages. During the first stage, the drone was on the ground with the rotors off for

177   ten minutes (G_NR). In the second stage, the drone was on the ground with the rotors

178   on for the next ten minutes (G_R). In the last stage the drone hovered at a fixed position

179   and fixed altitude of ten meters above the surface for ten minutes (FLY). A summary of

180   date and time of each test flight is given in Table 1. There are some deviations from the

181   G_NR, G_R and FLY routines. T1 was a pre-test so there was no FLY. Additionally,

182   due to high wind speeds and associated operational safety concerns, T9 and T13 had to

183   reduce the test time of FLY to 7 minutes and 5 minutes, respectively. Three vertical

184   profiles were made at the end of T10, T12, and T13, the details of which are provided

185   in Table 2. The main purpose of profiling during T10, T12 and T13 was to investigate:

186   1) the stability in the POPS instrument when profiling up and down as this is likely to

187   be a prime operating maneuver when flying scientific sorties in the future; 2) the

188   performance of the POPS at different vertical ascent and descent rates; and 3) the

189   accuracy of the POPS on the way up and way down which could conceivably be

190   influenced by turbulent disturbance by the rotors, particularly on vertical descents when

191   the aerosol inlet will be in the wake of the drone rotors. The test flights were all

192   performed at the Streatham campus of the University of Exeter (50.73N, 3.53W), UK.

3 Results

3.1 Comparison of POPS data against data from LASIC/CLARIFY-2017.

Figure 2 shows the mean PSD measured by the POPS and SMPS for the 20-day period, respectively. Figure 2 represents the whole size range of the two instruments as well as the fitted PSD from measurements with a wing-mounted PCASP-100X mounted on the UK's Bae146 FAAM aircraft from a flight during CLARIFY-2017 (Peers et al., 2019), which has been shown to be representative of biomass burning aerosol during the wider CLARIFY-2017 measurement campaign (Wu et al., 2020). That the POPS and SMPS show close overlap at the peak concentrations indicates that the counting statistics and the particle concentrations are similar between the instruments. The mean PSD measured by the POPS and SMPS shows reasonable agreement. Although the agreement is not as good as that demonstrated in other comparisons against SMPS instruments (e.g. Gao et al., 2016), any resulting errors in derived optical parameters are likely to be small provided the fit is reasonable over the 0.2-1.0 μm diameter range. Measurements of biomass burning aerosol over the Atlantic from the SAFARI-2000 campaign suggest that particles in this range contribute to 93% of the scattering at 0.55μm (e.g. Table 1, Haywood et al., 2003). The PSD from the wing-borne PCASP-100X that was operated on the FAAM bears a close resemblance to the SMPS and POPS PSDs except at particle sizes <0.2μm diameter and >0.7μm diameter. The discrepancy at particle sizes <0.2μm might be expected because the fits that are adopted

214   by Haywood et al. (2003) and Peers et al. (2019) do not account for these small particles

215   as they were developed with simplicity in mind for global general circulation models

216   and for satellite retrievals respectively. Aerosols >0.7μm diameter that were observed

217   by the POPS that were not present in the CLARIFY-2017 or SAFARI-2000 data may

218   well be generated by dust generation from the arid surface of Ascension Island or by

219   super-micron sea-salt from breaking waves. Taylor et al (2020) document the enhanced

220   influence of the oceanic component of aerosols in the marine boundary layer, but this

221   is not included in the CLARIFY-2017 or SAFARI-2000 log-normal fits which

222   represent biomass burning aerosols only. Thus, the POPS instrument appears to provide

223   a reasonably quantitative measure of optically active sub-micron biomass burning

224   aerosols.

225

226   We also investigated the overall particle number concentration from the POPS, and

227   examine the time series of the POPS measurements against some other key variables

228   measured by the SMPS and other instrumentation at the ARM mobile facility. The

229   upper panel of Figure 3a presents the 20-day intercomparison of the PNCs from the

230   POPS and SMPS, and panel 3b shows the ratio of the two concentration measurements

231   (POPS/SMPS). They show a good agreement between two instruments while the

232   geometric mean diameter (GMD) the of the size distribution (Figure 3c) is above

233   0.12μm. Again, this illustrates that the POPS instrument measures accumulation mode

234   aerosols reasonably accurately.

235

236 We would expect biomass burning aerosols to be associated with an increase in carbon

237 monoxide (CO; Haywood et al., 2003; Wu et al., 2020), and the concentrations

238 measured by both the POPS and SMPS instruments are well correlated with the CO

239 mass mixing ratio (as measured by a co-located CO analyzer – Figure 3d). The

240 concentration data also show some correlation with the AODs as measured by a co-

241 located AERONET Cimel sun-photometer (panel five, Figure 3), although this AOD is

242 a column measurement rather than a point measurement so the influence of vertical

243 profile will likely be important (e.g. Wu et al, 2020; Haywood et al, 2020).

3.2 Test flight results

245 To determine the impact of rotors and drone attitude on the POPS, we focus on the

246 comparison of PSD and PNC at three different stages: G_NR, G_R, and FLY. Table 3

247 summaries the mean PNC with standard deviation and the PNC percentage differences

248 of each flight at different stages.

249 3.2.1. Particle number concentration (PNC)

250 Compared with the mean PNC at G_NR, the mean PNC at G_R changed from -1% to

251 26%, and that at FLY changed from -1% to 63%, respectively. However, it is apparent

252 that the differences of PNCs are much lower in the cases T1, T2, T6, T7, and T10 (less

253 than 10%) in both stages. Figure 4 shows the probability density functions of PNC in

254 each case. The PNC at three stages of each case were separated into 15 bins. Unpaired

255 two-sample t-tests were selected to detect the similarity of the PNCs at different stages

256 as the t-test is the most popular parametric test for samples following normal

257   distribution for calculating the significance of a small sample size (De Winter, 2013).

258   Here the PNC of G_NR was set as the control group, while that of G_R and FLY was

259   set as the perturbation groups using the mean PNC at each stage every 30 seconds.

260   Before the t-test, the Levene's test was performed which is an inferential statistic used

261   to assess the equality of variances for a variable calculated for two or more groups

262   (Levene, 1960). If the Levene's test cannot be passed, then the unequal variances t-test,

263   which is a more conservative test, was be applied for the groups. The results (p value)

264   of the t-test of each test flight are shown in Table 4.

265

266   For a significance level (α) set as 0.05, there are 5 test flights that passed the t test in

267   both G_R and FLY stages (p value $\geq$ α), which means the PNC measured at G_R and

268   FLY stage corresponded well with those measured at G_NR. These test numbers have

269   been marked in green and bold italic font in Table 4. This result indicates that the impact

270   of rotors and UAV attitude was not significant in these five cases. The other three cases

271   (T8, T9, and T14) passed the t-test in the G_R stage, which are marked yellow and italic

272   font. The rest of test flights did not pass the t-test in either stage (marked red and

273   standard font). Through comparing the weather conditions, we find that the wind speed

274   (Table 4) was relatively lower (0.5-2.6m/s) in the cases which pass the t-test at both

275   stages. The wind speed in the Table 4 was provided from observations at Exeter airport

276   with one-hour resolution. During the actual experiment, when the wind speed was high,

277   visual observations by the drone pilot suggested that the drone swung from side to side

278   in the air, causing increased variability in the pitch, yaw and altitude of the drone. As

279   previously noted, on T9 and T13 the drone was forced to land early to ensure safety due

280   to the high (>7 m/s) instantaneous wind speed.

281

282   To determine the impact of wind speed on PNC observed by the POPS, the cases are

283   separated into 2 categories: low wind speed (w<2.6m/s) cases and high wind speed

284   (2.6<w<7.7m/s) cases. The PNC root mean square differences (RMSD) and mean

285   absolute differences (MAD) at G_R and FLY for all cases, low wind speed cases, and

286   high wind speed cases are given in the Table 5. For all cases, PNC RMSD is less than

287   10.2% at G_R and less than 26.2% at FLY, and MAD is less than 7.8% at G_R and less

288   than 19.1% at FLY. However, in the low wind cases, the RMSD and MAD fall to 2.4%

289   and 2.3% at G_R, and 5% and 3% at FLY, respectively. In contrast, RMSD and MAD

290   in the high wind cases increase to 12.6% and 10.9% at G_R, 31.4% and 26.3% at FLY,

291   respectively. The variability in the pitch, yaw and altitude of the drone also impacted

292   the orientation of the inlet of the POPS, which ideally should be perpendicular to the

293   horizontal plane. Variations in the orientation of the inlet led to uncertainties in the

294   sample flow rate. Table 6 shows mean sample flow rates with standard deviation at

295   G_NR, G_R, and FLY for all cases. It is clear that for G_NR, the mean flow rates were

296   constant across all tests and the standard deviation in the flow rates were very low.

297   Comparing with G_NR, the mean sample flow rate and the standard deviation were

298   almost unchanged with for G_R. This shows that operating the rotors alone didn't

299   impact the sample flow rate. However, while the mean flow rate during FLY was

300   identical to G_NR, the standard deviations increased during the FLY stage, particularly

301   for the tests under high windspeeds. The mean value of the standard deviation for low

302 windspeed cases was 0.13, while for the high windspeed cases was 0.21 which may

303 influence the accuracy of the POPS measurements.

304

305 3.2.2. The particle size distribution (PSD)

306 The PSDs at different stages and the mean PSDs ratios at G_R to G_NR and FLY to

307 G_NR of each test flight are shown in Figure 5, which indicates that the cases with high

308 similarity of PNCs (T1, T2, T6, T7, and T10) show agreement of the PSD. It also shows

309 that the differences of sub-micron sizes are less than those of super-micron sizes at G_R

310 and FLY. Therefore, the size distribution was separated into two modes, the

311 accumulation mode ($0.1 \leq d \leq 1.0\mu m$) and the coarse mode ($d > 1.0\mu m$), to make a

312 statistical analysis. Table 7 summaries the PSDs percentage differences for two modes

313 at G_R and FLY for each case. The PSDs RMSD and MAD for two modes at G_R and

314 FLY for all cases, low wind cases, and high wind cases are given in Table 7. The

315 percentage differences of the PSDs are less than 5.4% and 14.9% in low wind cases at

316 the accumulation mode at G_R and FLY, respectively, while the variation in the PSD in

317 the coarse mode is perhaps due to lower counting statistics at these sizes. In contrast

318 PSDs of other cases show differences across the whole spectrum. Even in the

319 accumulation mode, the differences of the PSDs between FLY and G_NR are up to 53.2%

320 in the case T8. PSDs RMSD and MAD at the accumulation mode are 3.4% and 2.7%

321 respectively at G_R in the low wind speed cases, but up to 12.9% and 11.1% at G_R in

322 the high wind speed cases. These statistics again indicate that impacts of rotors and

323 UAV attitude on the POPS measurements appear to be reduced in low wind speeds

324 relative to higher wind speeds. PSD RMSDs and MADs at the coarse mode at G_R,

325 and at the accumulation and coarse mode at FLY show the same result. Generally

326 speaking, RMSDs and MADs indicate the impact of rotors and UAV attitude on the

327 POPS operated in accumulation mode is lower than when in coarse mode, for all cases.

328 RMSDs in accumulation mode were 10.6% at G_R and 21.6% at FLY, while those in

329 coarse mode were 32.2% and 49.5% for all cases. MADs showed the same trend as

330 RMSDs. In the absence of independent multi-stage meteorological tower

331 measurements (e.g. Ahn, 2019), it is difficult to assess how much of the variability in

332 PNCs and PSDs is real, particularly when the drone is flying; there may be changes in

333 PNC with altitude when compared to the surface PNCs owing to surface deposition.

334 Alternatively, there may be trends in the particle concentrations that occur during the

335 entire measurement period which spanned around 30 minutes duration. We determine

336 trends in the G_NR and G_R statistics by determining the mean slope (particles / s)

337 during the operating periods; only flights T4 and T6 show trends of greater than 0.1

338 particles per second (6 particles / minute) when averaged over both G_NR and G_R.

339 Figure 4 shows that there is potentially an increase in the concentrations that are

340 measured during T4, and that there is potentially a bi-modal number concentration

341 measured during the G_NR sampling period for T6. As no trends are evident for the

342 other flights, it can be inferred that there is no evidence of a systematic significant trend

343 in atmospheric concentrations across all flights; any such trends are likely to be random.

344 However, a potential solution to any concern would be to change the three stage

345 sequence from G_NR, G_R, FLY to a five stage sequence of G_NR, G_R, FLY, G_R

346   and G_NR. This sequence is suggested for future investigations.

347

348   3.2.3. The PNC during vertical profiles

349   Figure 6 presents the results of the vertical profile runs in T10, T12, and T13. The mean

350   PNC with standard deviation on the way up and down are shown in Table 8. The PNC

351   measured on the way up and way down show agreement. The best agreement is found

352   in the high number concentration, low wind-speed case (T10), where the PNCs differ

353   by an average of 0.5% between ascent and descent. Even in the high wind-speed cases

354   when the variability might be expected to be largest owing to changes in the pitch and

355   yaw of the drone, general agreement is found indicating that the vertical speed of the

356   drone (which was approximately 0.5 to 1m/s) does not appear to have a significant

357   impact. Note that the vertical profiles do indicate some variability in the vertical

358   distribution with PNCs ranging from 1207 ± 83 cm^{-3}, 69 ± 14 cm^{-3}, and 90 ± 11 cm^{-3} close to

359   the surface to 1189 ± 107 cm^{-3}, 55 ± 11 cm^{-3}, and 72 ± 15 cm^{-3} in ascent and 1395 ± 83 cm^{-3},

360   69 ± 5 cm^{-3}, and 89 ± 6 cm^{-3} close to the surface to 1201 ± 101 cm^{-3}, 54 ± 12 cm^{-3}, and 82 ± 13

361   cm^{-3} in descent for flights T10, T12 and T13. The close to surface data were collected

362   by the UAV-mounted POPS when the drone was 1-3 meters above the surface. This

363   variability with height emphasizes the utility of small, instrumented UAVs for

364   measuring PNCs and PSDs at low altitudes; measurements at such altitudes are

365   impossible to probe with heavily equipped atmospheric research aircraft operating

366   under standard aviation safety protocols.

4 Conclusions

We have investigated the performance of POPS against a reference SMPS instrument while on the ground and also while operated on a quadcopter drone, DJI Matrice 200 V2, which is the first documented test of the performance of a POPS instrument on a UAV. The investigation includes two parts. The first is a long-term comparison between the POPS and other instruments during the CLARIFY-2017/LASIC and SAFARI-2000 project. The results show that the PNC measured by the POPS and that measured by the SMPS and PCASP indicate agreement in the optically important size range centred at around 0.3μm diameter. This indicates that despite its small size, when operating under controlled conditions on the ground, the POPS instrument performs relatively well. In the second part, we tested the impact of drone's rotors and, indirectly the attitude of the drone, on the performance of the POPS with a focus on two aspects, the PNC and PSD. We found RMSDs and MADs in PNC when operating a POPS on a small quad-copter to be less than 10.2% and 7.8%, respectively, when operating on the ground, and less than 26.2% and 19.1%, respectively, at 10m altitude under wind speed conditions of up to 7.7m/s. For wind speed of less than 2.6m/s, RMSDs and MADs fell to 2.4% and 2.3% when operating on the ground, and to 5% and 3% at 10m altitude. We also found no statistical difference in PNC when operating the UAV in either ascent or descent. As for the PSD, the accumulation mode aerosol size distributions were relatively invariant between measurements at the surface and measurements at 10m altitude with RMSD and MAD of less than 21.6% and 15.7%, respectively. The

differences between coarse mode super-micron aerosols measured at the surface and at 10m altitude were universally greater than those measured at the surface with a RMSD and MAD approaching 49.5% and 40.4%, but it is unclear whether this is due to loss of coarse mode aerosol particles to the surface or whether this is due to interference from the rotors. This impact appears to be most prevalent at the larger end of the POPS size range. These results suggest that, when the wind-speed is modest, the POPS and UAV and very simple inlet combination examined here appears able to measure the aerosol PSD and PNC with reasonable fidelity, particularly for sub-micron aerosols.

In follow-up scientific observations, the POPS deployed on the quadcopter drone will be used to measure the aerosol properties in the atmospheric boundary layer (ABL) under polluted condition. Concentration of pollutants in the ABL frequently have a strong correlation with atmospheric stability (Wang et al., 2013, Chambers et al., 2015) with stable conditions leading to the build-up of pollutants in the ABL. Wind-speeds are frequently low in stable conditions due to the lack of convection driven turbulence. Because these future measurements are likely under stable, non-turbulent conditions, wind-speed effects are not likely to cause significant problems. For other applications of the POPS on a quadcopter drone, such as the dispersion of pollutants in down-wind driven plumes, attention should be paid to the influence of the higher wind speeds.

Acknowledgements: This work was supported by the Chinese University of Hong Kong – University of Exeter Joint Centre for ENvironmental SUstainability and REsilience (ENSURE) programme; ZL, MO, JH, KA, JS, TH, JC and SY would like

410 to thank ENSURE for their financial support. JH, ZL and HC would also like to

411 acknowledge NERC SWAAMI (South West Asian Aerosol Monsoon Interactions)

412 grants NE/L013878/1 and NE/L013886/1 for partial funding of the research.

413

414

415

416

417

418

419

420

421

422

423

424

425

426

427

428

429

430

431

References

Ahn, K-H, Aerosol 3D Profiling Using Compact Particle Measuring Instruments with Balloon and Drone System, *7th International Symposium on Ultrafine Particles, Air Quality and Climate (2019)*, DOI: 10.5445/IR/1000096749,

Albrecht, B. A. (1989). Aerosols, cloud microphysics, and fractional cloudiness. *Science, 245*(4923), 1227-1230.

Atkinson, D. B., Pekour, M., Chand, D., Radney, J. G., Kolesar, K. R., Zhang, Q., Setyan, A., O'neill, N. T. & Cappa, C. D. 2018. Using spectral methods to obtain particle size information from optical data: applications to measurements from CARES 2010. Atmospheric Chemistry and Physics, 18, 5499-5514.

Atkinson, D. B., Radney, J. G., Lum, J., Kolesar, K. R., Cziczo, D. J., Pekour, M., Zhang, Q., Setyan, A., Zelenyuk, A. & Cappa, C. D. 2015. Aerosol optical hygroscopicity measurements during the 2010 CARES campaign. Atmospheric Chemistry and Physics, 15, 4045–4061.

Bezantakos, S., Schmidt-Ott, F., Biskos, G., 2018. Performance evaluation of the cost-effective and lightweight Alphasense optical particle counter for use onboard unmanned aerial vehicles. Aerosol Sci. Technol. 52, 385–392.

Bellouin, N., Boucher, O., Haywood, J., & Reddy, M. S. (2005). Global estimate of aerosol direct radiative forcing from satellite measurements. Nature, 438(7071), 1138-1141.

Boucher, O., D. Randall, P. Artaxo, C. Bretherton, G. Feingold, P. Forster, V.-M. Kerminen, Y. Kondo, H. Liao, U. Lohmann, P. Rasch, S.K. Satheesh, S. Sherwood, B. Stevens and X.Y. Zhang, 2013: Clouds and Aerosols. In: Climate Change 2013: The Physical Science Basis. Contribution of Working Group I to the Fifth Assessment Report of the Intergovernmental Panel on Climate Change [Stocker, T.F., D. Qin, G.-K. Plattner, M. Tignor, S.K. Allen, J. Boschung, A. Nauels, Y. Xia, V. Bex and P.M. Midgley (eds.)]. Cambridge University Press, Cambridge, United Kingdom and New York, NY, USA.

Burkart, J., Steiner, G., Reischl, G., Moshammer, H., Neuberger, M., & Hitzenberger, R. (2010). Characterizing the performance of two optical particle counters (Grimm OPC1. 108 and OPC1. 109) under urban aerosol conditions. Journal of Aerosol Science, 41(10), 953-962.

Chambers, S. D., Wang, F., Williams, A. G., Xiaodong, D., Zhang, H., Lonati, G., Crawford, J., Griffiths, A. D., Ianniello, A. & Allegrini, I. 2015. Quantifying the influences of atmospheric stability on air pollution in Lanzhou, China, using a radon-based stability monitor. Atmospheric Environment, 107, 233-243.

De Winter, J. C. 2013. Using the Student's t-test with extremely small sample sizes. Practical Assessment, Research, and Evaluation, 18, 10.

Gao, R., Perring, A., Thornberry, T., Rollins, A., Schwarz, J., Ciciora, S. & Fahey, D. 2013. A high-sensitivity low-cost optical particle counter design. Aerosol Science and Technology, 47, 137-145.

Gao, R., Telg, H., Mclaughlin, R., Ciciora, S., Watts, L., Richardson, M., Schwarz, J., Perring, A., Thornberry, T. & Rollins, A. 2016. A light-weight, high-sensitivity particle spectrometer for PM2. 5 aerosol measurements. Aerosol Science and Technology, 50, 88-99.

475 Gu Y. and Yim S.H.L. (2016). The air quality and health impacts of domestic trans-boundary
476   pollution in various regions of China. Environment International, 97, 117-124.
477 Gu Y., Wong T.W., Law S.C.K., Dong G.H., Ho K.F., Yang Y., Yim S.H.L. (2018). Impacts of
478   Sectoral Emissions in China and the Implications: Air Quality, Public Health, Crop
479   Production, and Economic Costs. Environmental Research Letters, 13, 8.
480 Gu Y., Zhang W., Yang Y., Wang C., Streets D.G., Yim S.H.L. (2020). Assessing outdoor air
481   quality and public health impact attributable to residential black carbon emissions in
482   rural China. Resources, Conservation and Recycling, 159, 104812.
483 Haywood, J., & Boucher, O. (2000). Estimates of the direct and indirect radiative forcing due to
484   tropospheric aerosols: A review. Reviews of geophysics, 38(4), 513-543.
485 Haywood, J., Francis, P., Dubovik, O., Glew, M. & Holben, B. 2003a. Comparison of aerosol
486   size distributions, radiative properties, and optical depths determined by aircraft
487   observations and Sun photometers during SAFARI 2000. Journal of Geophysical
488   Research: Atmospheres, 108.
489 Haywood, J. M., Osborne, S. R., Francis, P. N., Keil, A., Formenti, P., Andreae, M. O. & Kaye,
490   P. H. 2003b. The mean physical and optical properties of regional haze dominated by
491   biomass burning aerosol measured from the C-130 aircraft during SAFARI 2000.
492   Journal of Geophysical Research: Atmospheres, 108.
493 Haywood, J.M., S. J. Abel, P. Barrett, N. Bellouin, A. Blyth, K.N. Bower, M. Brooks, K. Carslaw,
494   H. Coe, M. Cotterell, I. Crawford, N. Davies, B. Dingley, P. Field, P. Formenti, H. Gordon,
495   M. de Graaf, R. Herbert, B. Johnson, A.C. Jones, F. Malavelle, D.G. Partridge, F. Peers,
496   J. Redemann, P. Stier, J. Taylor, R. Wood, H.H. Wu, P. Zuidema. Overview of the
497   CLoud-Aerosol-Radiation Interaction and Forcing: Year-2017 (CLARIFY-2017)
498   measurement campaign, acp-2020-729, Atmos Chem Phys Diss, 2020.
499 Horvath, H. (1981). Atmospheric visibility. Atmospheric Environment (1967), 15(10-11), 1785-
500   1796.
501 Huebert, B. J., Lee, G., & Warren, W. L. (1990). Airborne aerosol inlet passing efficiency
502   measurement. Journal of Geophysical Research: Atmospheres, 95(D10), 16369-
503   16381.
504 IPCC: Climate Change 2013: The Physical Science Basis. Contri- bution of Working Group I to
505   the Fifth Assessment Report of the Intergovernmental Panel on Climate Change,
506   Cambridge University Press, Cambridge, United Kingdom and New York, NY, USA, 2013.
507 Jimenez, J.L., Canagaratna, M.R., Donahue, N.M., Prevot, A.S.H., Zhang, Q., Kroll, J.H.,
508   DeCarlo, P.F., Allan, J.D., Coe, H., Ng, N.L. and Aiken, A.C., 2009. Evolution of organic
509   aerosols in the atmosphere. Science, 326(5959), pp.1525-1529.
510 Lack, D. & Cappa, C. 2010. Impact of brown and clear carbon on light absorption enhancement,
511   single scatter albedo and absorption wavelength dependence of black carbon.
512   Atmospheric Chemistry and Physics, 10, 4207.
513 Levene, H. 1960. Robust tests for equality of variances. Ingram Olkin, Harold Hotelling, et alia.
514   Contributions to Probability and Statistics: Essays in Honor of Harold Hotelling.
515   Stanford University, 278-292.
516 Li, N. Hao, M. Phalen, R. Hinds, W. and Nel, N. "Particulate air pollutants and asthma: a
517   paradigm for the role of oxidative stress in PM-induced adverse health effects." Clinical
518   immunology 109, no. 3 (2003): 250-265.

Liu Z., Ming Y., Zhao C., Lau N.C., Guo J., Bollasina M., Yim S.H.L. (2019a). Contribution of local and remote anthropogenic aerosols to a record-breaking torrential rainfall event in Guangdong Province, China. Atmospheric Chemistry and Physics, 20, 223-241.

Liu Z., Ming Y., Wang L., Bollasina M., Luo M., Lau N.C., Yim S.H.L. (2019b). A Model Investigation of Aerosol-Induced Changes in the East Asian Winter Monsoon. Geophysical Research Letters, 46(16), 10186-10195.

Liu Z., Yim S.H.L., Wang C., Lau N.C. (2018). The impact of the aerosol direct radiative forcing on deep convection and air quality in the Pearl River Delta region. *Geophysical Research Letters*, 45(9), 4410-4418.

Peers, F., Francis, P., Fox, C., Abel, S.J., Szpek, K., Cotterell, M.I., Davies, N.W., Langridge, J.M., Meyer, K.G., Platnick, S.E. and Haywood, J.M., 2019. Observation of absorbing aerosols above clouds over the south-east Atlantic Ocean from the geostationary satellite SEVIRI–Part 1: Method description and sensitivity. *Atmospheric Chemistry and Physics*, 19, 9595–9611, 2019 https://doi.org/10.5194/acp-19-9595-2019.

Ruzer, L. S. & Harley, N. H. 2012. Aerosols handbook: measurement, dosimetry, and health effects, CRC press.

Sang-Nourpour, N., & Olfert, J. S. (2019). Calibration of optical particle counters with an aerodynamic aerosol classifier. *Journal of Aerosol Science*, 138, 105452.

Sanchez-Marroquin, A., Hedges, D. H. P., Hiscock, M., Parker, S. T., Rosenberg, P. D., Trembath, J., Walshaw, R., Burke, I. T., McQuaid, J. B., and Murray, B. J.: Characterisation of the filter inlet system on the FAAM BAe-146 research aircraft and its use for size-resolved aerosol composition measurements, Atmos. Meas. Tech., 12, 5741–5763, https://doi.org/10.5194/amt-12-5741-2019, 2019.

Shi C., Nduka I.C., Yang Y., Huang Y., Yao R., Zhang H., He B., Xie C., Wang Z., Yim S.H.L. (2019). Characteristics and Meteorological Mechanisms of Transboundary Air Pollution in A Persistent Heavy PM2.5 Pollution Episode in Central-East China. *Atmospheric Environment*, 223, 117239.

Taylor, J. W., Wu, H., Szpek, K., Bower, K., Crawford, I., Flynn, M. J., Williams, P. I., Dorsey, J., Langridge, J. M., Cotterell, M. I., Fox, C., Davies, N. W., Haywood, J. M., and Coe, H.: Absorption closure in highly aged biomass burning smoke, *Atmospheric Chemistry and Physics*, 20, 11201–11221, https://doi.org/10.5194/acp-20-11201-2020, 2020.

Twomey, S. (1977). The influence of pollution on the shortwave albedo of clouds. *Journal of the atmospheric sciences*, 34(7), 1149-1152.

Wang, F., Zang, H., Ancora, M. & Deng, X. 2013. Measurement of atmospheric stability index by monitoring radon natural radioactivity. *China Environmental Science*, 33, 594-598.

Wu, H., J.W. Taylor, K. Szpek, P.I. Williams, M. Flynn, J. Langridge, J.D. Allan, J. Pitt, S. Abel, J. Haywood, H. Coe, Vertical and temporal variability of the properties of transported biomass burning aerosol over the southeast Atlantic during CLARIFY-2017, *ACPD.*.

Yim S.H.L., Gu Y., Shapiro M., Stephens B. (2019). Air quality and acid deposition impacts of local emissions and transboundary air pollution in Japan and South Korea. *Atmospheric Chemistry and Physics*, 19, 13309-13323.

Yim S.H.L. (2020). Development of a 3D Real-Time Atmospheric Monitoring System (3DREAMS) Using Doppler LiDARs and Applications for Long-Term Analysis and Hot-and-Polluted Episodes. *Remote Sensing* 12 (6), 1036.

563 Yin, Y., Levin, Z., Reisin, T. G. & Tzivion, S. 2000. The effects of giant cloud condensation nuclei
564   on the development of precipitation in convective clouds—A numerical study.
565   *Atmospheric Research*, 53, 91-116.
566 Yu, P., Rosenlof, K. H., Liu, S., Telg, H., Thornberry, T. D., Rollins, A. W., Portmann, R. W., Bai,
567   Z., Ray, E. A. & Duan, Y. 2017. Efficient transport of tropospheric aerosol into the
568   stratosphere via the Asian summer monsoon anticyclone. *Proceedings of the National*
569   *Academy of Sciences*, 114, 6972-6977.
570 Zuidema, P., Sedlacek III, A.J., Flynn, C., Springston, S., Delgadillo, R., Zhang, J., Aiken, A.C.,
571   Koontz, A. and Muradyan, P., 2018. The Ascension Island boundary layer in the remote
572   southeast Atlantic is often smoky. *Geophysical Research Letters*, 45(9), pp.4456-4465.
573 Zuidema, P., Redemann, J., Haywood, J., Wood, R., Piketh, S., Hipondoka, M. and Formenti,
574   P., 2016. Smoke and clouds above the southeast Atlantic: Upcoming field campaigns
575   probe absorbing aerosol's impact on climate. *Bulletin of the American Meteorological*
576   *Society*, 97(7), pp.1131-1135.

577
578
579
580
581
582
583
584
585
586
587
588
589
590
591
592
593
594
595
596
597
598
599
600
601
602
603
604
605
606

607

608 **Figure 1.** The DJI Matrice 200 V2 with the POPS (white box at the left bottom of the fuselage).
609 The red oval shows the inlet tube leading to the POPS.

610

611

612
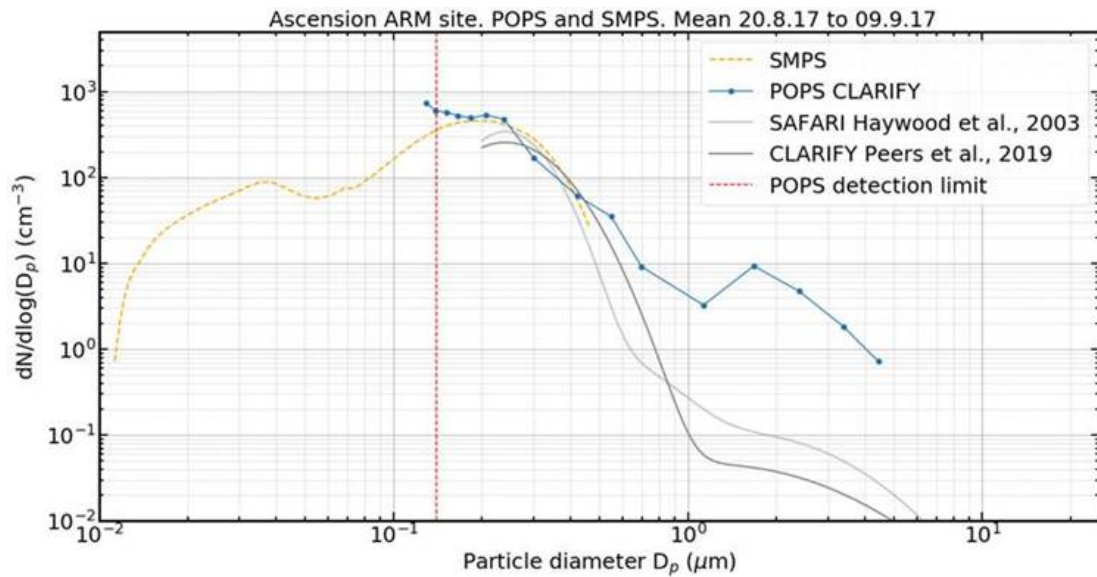
613 **Figure 2.** PSDs from POPS, SMPS, and data fitted to a wing-mounted PCASP from CLARIFY-
614 2017 and SAFARI-2000. POPS and SMPS data were collected at the ARM mobile site on Ascension
615 Island from 20th of August to 9th of September 2017.The PCASP data from CLARIFY were
616 collected from a flight on 4th of September 2017 (Peers et al., 2019). The PCASP data from SAFARI-
617 2000 represent a mean from 11 flights performed off the coast of Namibia (Haywood et al., 2003).
618 Note that the CLARIFY-210 and SAFARAI-2000 PCASP distributions are 'scaled' to the SMPS
619 size distribution to aid comparison. The POPS and SMPS values are not scaled.
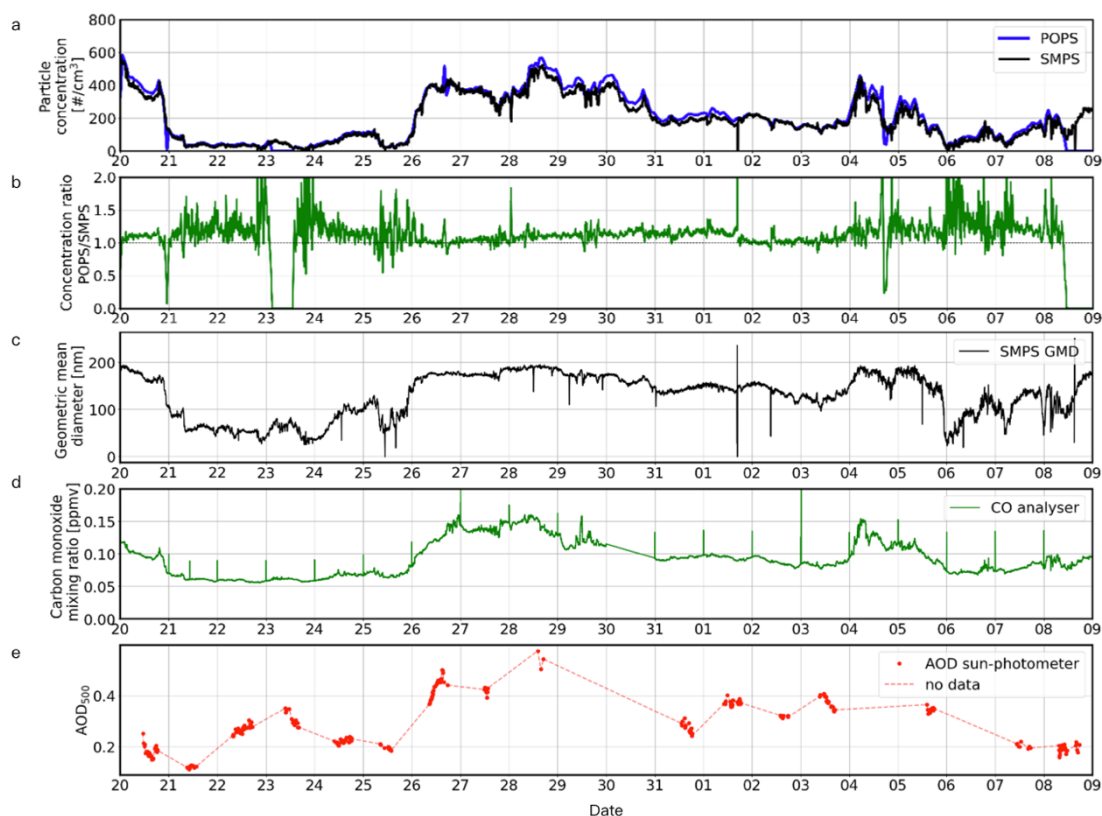
620
621 **Figure 3.** From top to bottom. (a) SMPS and POPS total particle concentration. The number
622 distribution is calculated over the range of bins that overlap between the two instruments
623 (approximately 120 - 450nm diameter). (b) Ratio of POPS to SMPS total particle concentration
624 derived from (a). (c) Geometric mean diameter from SMPS. (d) Carbon monoxide mixing ratio from
625 Los Gatos Research CO analyser, and (e) AOD from Cimel sun- photometer. Spikes in the CO data
626 occur at the beginning of each day when the instrument is in calibration mode.
627
628
629
630
631
632
633
634
635
636
637
638
639
640
641
642
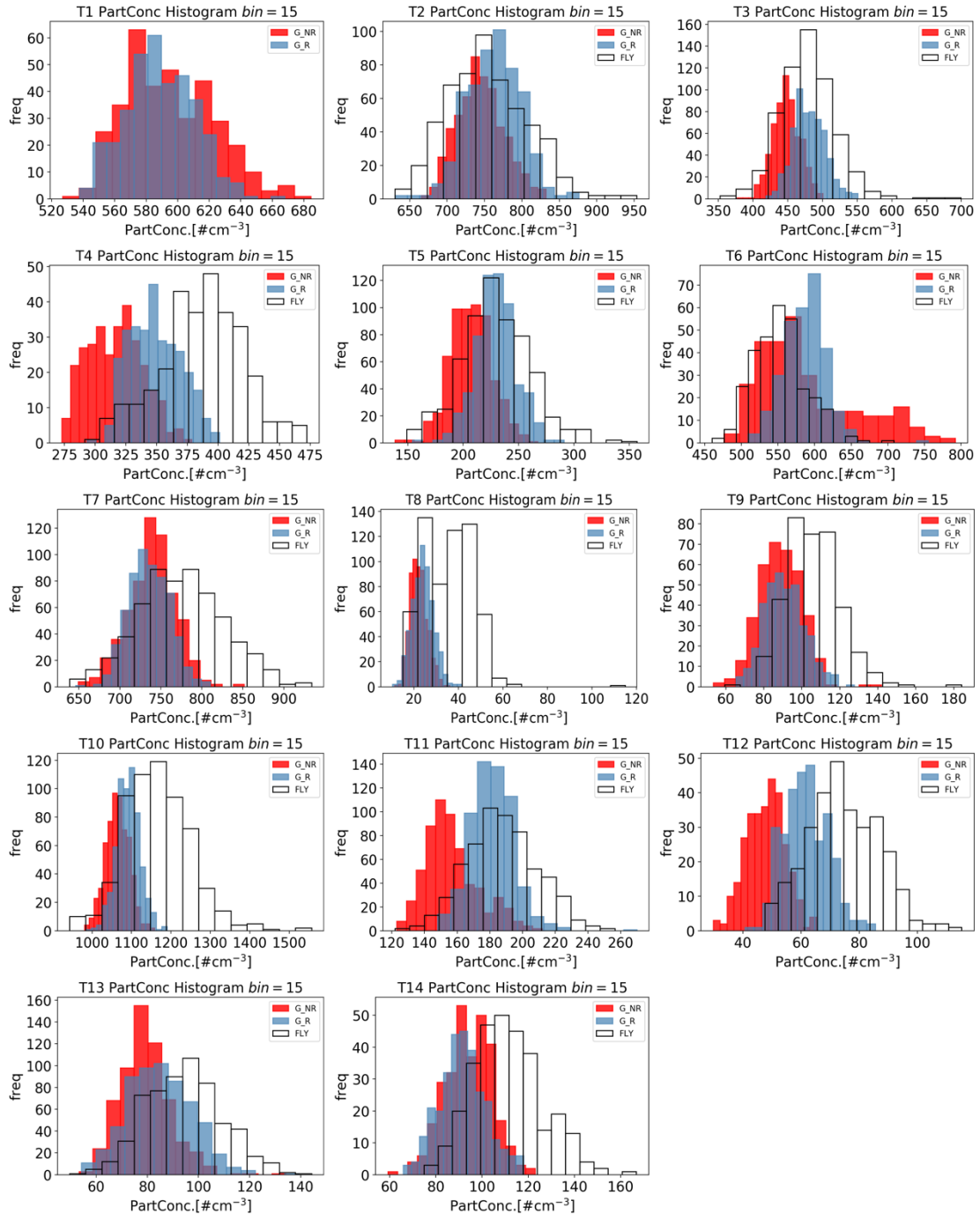
Figure 4. Probability density functions of PNCs in each case. The bin number was set to 15 for all stages. Red represents the G_NR, blue represents G_R, and white represents FLY.

654
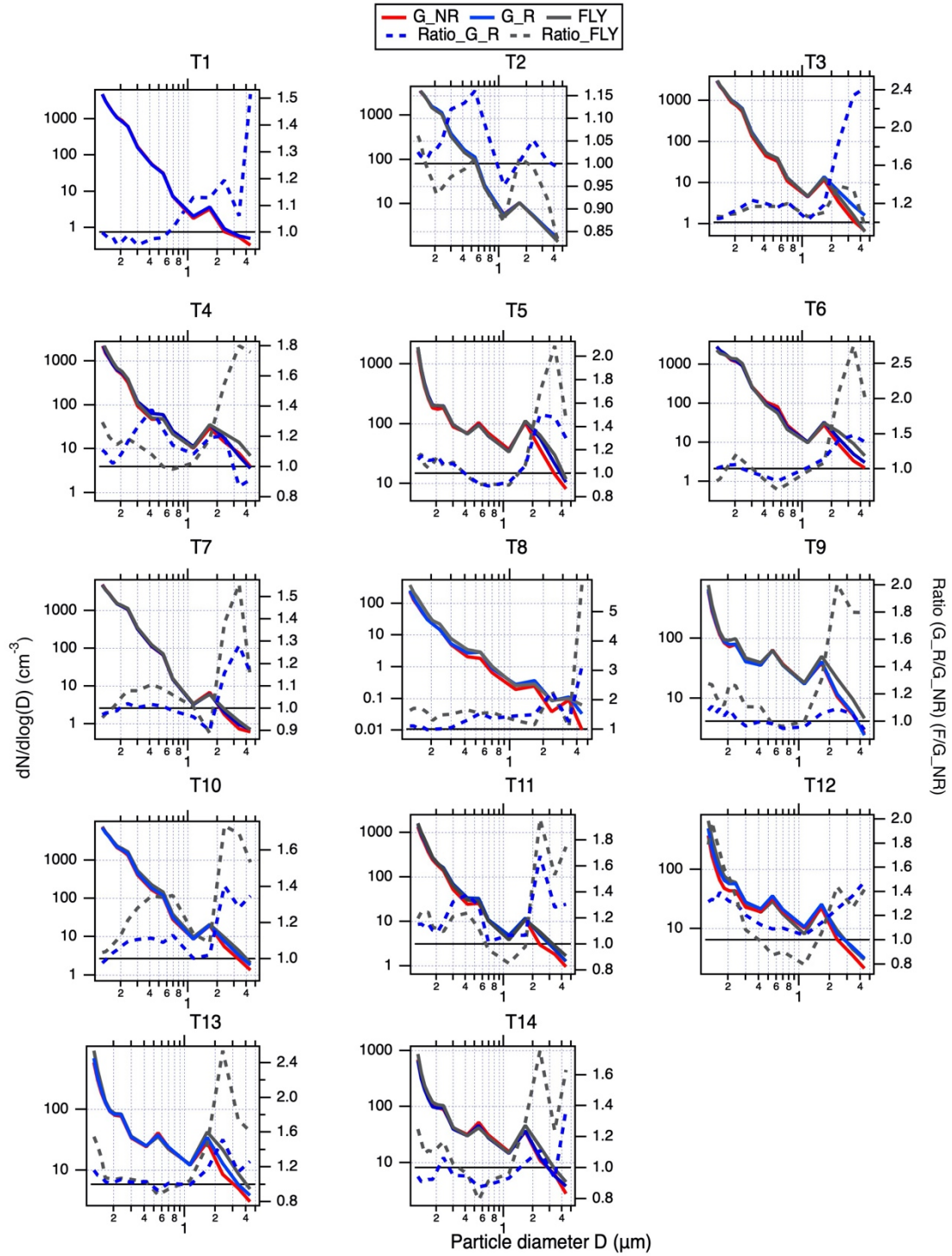
Figure 5. Particle size distribution at three stages: the drone on the ground with rotors off (G_NR) (red line), on the ground with rotors on (G_R) (blue line) and flying at 10m (FLY) (grey line), in each POPS test. The ratios of the PSD at G_R to G_NR (blue dash line) and at FLY to G_NR (grey dash line) of each flight are given in each plot.

659

660
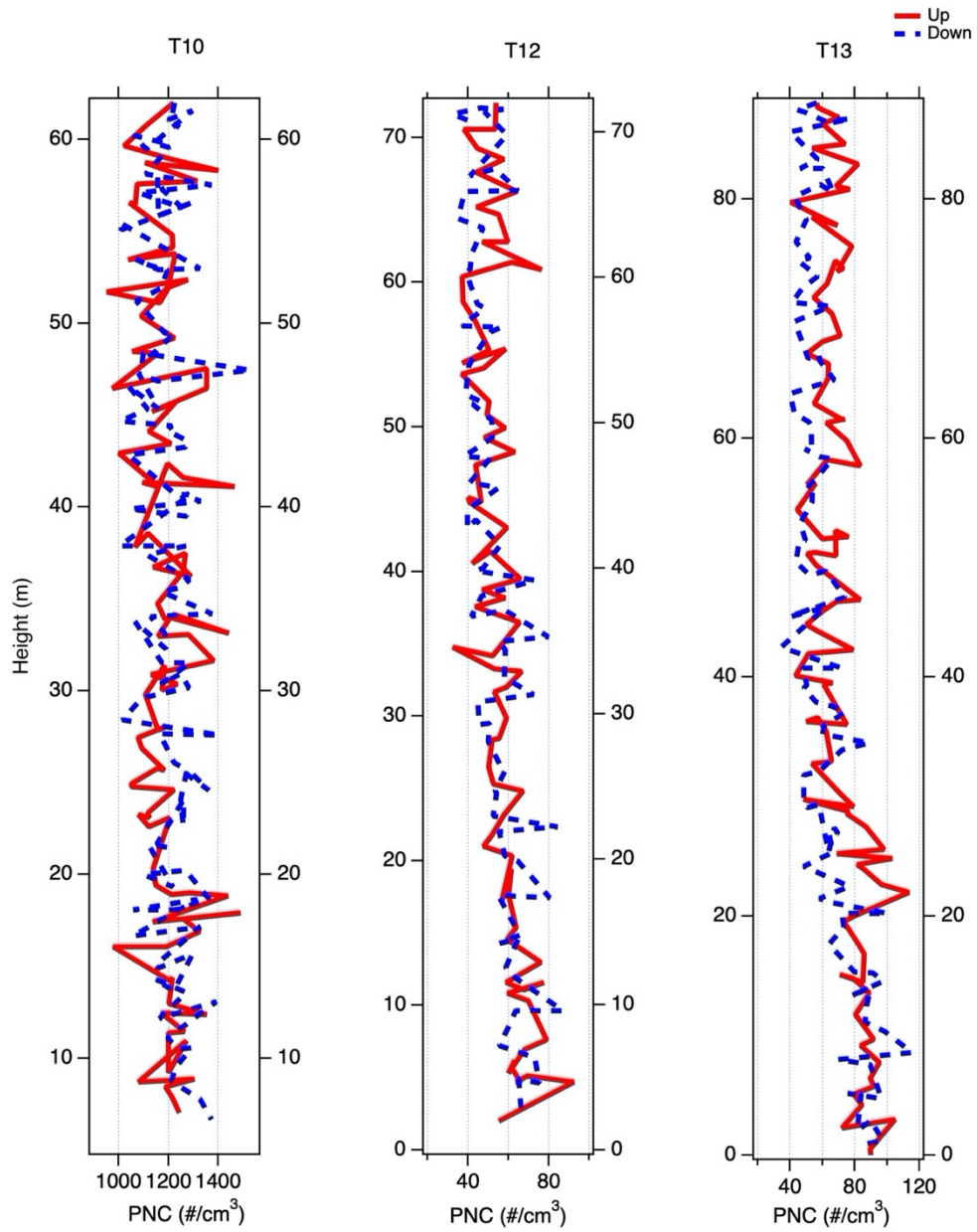
Figure 6. Vertical profiles of the particle number concentration in the profile runs of T10, T12, and T13. The red line shows the observed concentration in the way up and the blue dash line shows that in the way down, respectively.

	Date	Time
T1	18/Nov/2019	16:07 - 16:30
T2	19/Nov/2019	17:00 - 17:35
T3	20/Nov/2019	14:20 - 15:10
T4	25/Nov/2019	10:36 - 11:15
T5	26/Nov/2019	15:21 - 16:00
T6	28/Nov/2019	11:08 - 11:46
T7	2/Dec/2019	11:45 – 12:31
T8	30/Jan/2020	11:49 – 12:34
T9	4/Feb/2020	10:41 – 11:15
T10	7/Feb/2020	11:57 – 12:44
T11	12/Feb/2020	16:35 – 17:26
T12	26/Feb/2020	14:36 – 17:27
T13	3/Mar/2020	11:24 – 12:06
T14	9/March/2020	11:55 – 12:28

Table 1. Summary of the dates and time of each test flight.

	Initial Height (m)	End Height (m)	Vertical Speed (m/s)
T10	5	60	0.5
T12	5	70	1
T13	2	90	1

Table 2. Summary of the initial and end heights and vertical speed of each vertical profile.

	Date	Particle Number Concentrations (PNCs) (cm^{-3})			Percentage Difference (%)	
		G_NR	G_R	FLY	G_R	FLY
T1	18/Nov/2019	597±30	587±22	n/a	-1.7	n/a
T2	19/Nov/2019	741±52	767±35	742±31	3.5	0.1
T3	20/Nov/2019	442±48	479±23	478±40	8.4	8.1
T4	25/Nov/2019	317±36	349±21	385±30	10.1	21.5
T5	26/Nov/2019	207±19	228±18	230±31	10.1	11.1
T6	28/Nov/2019	567±50	580±30	561±41	2.3	-1.1
T7	2/Dec/2019	753±30	745±24	760±55	-1.1	0.9
T8	30/Jan/2020	22±4	24±5	36±11	9.1	63.6
T9	4/Feb/2020	87±11	91±11	105±19	4.6	20.7
T10	7/Feb/2020	1063±29	1092±29	1169±84	2.7	9.9
T11	12/Feb/2020	156±16	181±13	187±21	16.0	19.9
T12	26/Feb/2020	50±7	63±9	74±11	26	48
T13	3/Mar/2020	79±10	86±13	102±13	8.9	29.1
T14	9/March/2020	95±12	90±10	108±14	-5.3	13.7

Table 3. Summary of the PNCs of each test flight at three stages. n/a = not applicable. The numbers denoted by ±x represent the standard deviation in the PNCs during the measurement time period.

	Surface Wind Speed (m/s)	T test P value	
		G_R	FLY
T1	0.5	0.2	n/a
T2	2.6	0.3	0.6
T3	5.7	2e-9	2e-7
T4	3.6	8e-5	2e-7
T5	6.7	2e-9	2e-6
T6	1.5	0.9	0.2
T7	1	0.9	0.3
T8	4.1	0.05	3e-6
T9	7.7	0.2	1e-10
T10	n/a	0.7	0.2
T11	n/a	2e-5	5e-6
T12	n/a	4e-10	1e-6
T13	n/a	0.02	1e-14
T14	n/a	0.2	1e-5

Table 4. Summary of the dates, time, wind speed, and t test results (p value) of each test flight. Wind speed values (at 1.5m) are the wind speed in the hour closest to the experiment time. From T10 to T14 the wind speed data is not available (n/a) because the instrument recording the data had broken. Flights highlighted in green and bold italic font indicate that the results are not significantly different at 5% significance. Flights marked in yellow and italic font indicate that the PNC on the ground with the rotor on are not significantly different from G_NR, and flights marked in red and standard font indicate that there are significant differences in both G_R and FLY when compared to G_NR.

	PNC RMSD (%)	
	G_R	FLY
All cases	10.2	26.2
Low wind speed cases (w<2.6m/s)	2.4	5
High wind speed cases (2.6<w<7.7m/s)	12.6	31.4
	PNC MAD (%)	
	G_R	FLY
All flights	7.8	19.1
Low wind speed cases (w<2.6m/s)	2.3	3
High wind speed cases (2.6<w<7.7m/s)	10.9	26.3

Table 5. Summary of RMSD and MAD for all cases, low wind cases, and high wind cases.

	Surface Wind Speed (m/s)	Sample flow rate (cm^3/s)		
		G_NR	G_R	FLY
T1	0.5	3.04±0.04	3.03±0.04	n/a
T2	2.6	3.04±0.04	3.04±0.05	3.03±0.12
T3	5.7	3.03±0.04	3.03±0.06	3.03±0.20
T4	3.6	3.04±0.04	3.03±0.05	3.03±0.16
T5	6.7	3.02±0.04	3.02±0.04	3.00±0.26
T6	1.5	3.02±0.04	3.03±0.04	3.03±0.15
T7	1	3.03±0.03	3.03±0.05	3.03±0.17
T8	4.1	3.03±0.03	3.03±0.04	2.99±0.28
T9	7.7	3.03±0.04	3.03±0.05	3.02±0.21
T10	n/a	3.02±0.04	3.02±0.04	3.03±0.19
T11	n/a	3.02±0.04	3.02±0.04	3.03±0.22
T12	n/a	3.02±0.03	3.02±0.04	3.04±0.16
T13	n/a	3.02±0.04	3.03±0.04	3.03±0.23
T14	n/a	3.02±0.04	3.02±0.05	3.00±0.17

Table 6. Summary of the sample flow rates of each test flight at three stages. n/a = not applicable. The numbers denoted by ±x represent the standard deviation in the sample flow rates during the measurement time period.

	Mean Percentage Difference (%)			
	G_R (%)		FLY (%)	
	Accumulation	Coarse	Accumulation	Coarse
T1	-2.1	17.5	n/a	n/a
T2	5.4	1.6	-0.7	-7.0
T3	10.8	67.4	9.7	17.5
T4	13.3	6.8	15.0	38.3
T5	7.7	19.5	6.4	35.6
T6	-0.8	22.0	-3.6	61.8
T7	-0.3	7.5	3.3	17.2
T8	11.6	83.0	53.2	123.1
T9	4.2	0.9	15.6	48.0
T10	4.9	19.8	14.9	42.4
T11	18.0	23.8	16.8	33.9
T12	25.2	23.0	43.2	14.8
T13	4.2	18.4	13.9	55.5
T14	-5.1	4.5	7.3	29.9
	RMSD (%)			
	G_R		FLY	
	Accumulation	Coarse	Accumulation	Coarse
All cases	10.6	32.2	21.6	49.5
Low wind speed cases (w<2.6m/s)	3.4	15.8	7.8	38.6
High wind speed cases (2.6<w<7.7m/s)	12.9	38.5	25.4	53.6
	MAD (%)			
	G_R		FLY	
	Accumulation	Coarse	Accumulation	Coarse
All cases	8.1	22.6	15.7	40.4
Low wind speed cases (w<2.6m/s)	2.7	13.7	5.6	32.1
High wind speed cases (2.6<w<7.7m/s)	11.1	27.5	20.1	44.1

Table 7. Summary of mean percentage differences of size distribution between G_NR and G_R, and G_NR and FLY of each flight. The size distributions are separated into two modes: accumulation mode ($0.1 \leq d \leq 1\mu m$) and coarse mode ($d > 1\mu m$).

	Mean PNCs (cm^{-3})	
	Up	Down
T10	1189±107	1201±101
T12	55±11	54±12
T13	72±15	82±13

Table 8. Mean PNC with standard deviations on the way up and down in three vertical profile runs.